Applied Catalysis B: Environmental 180 (2016) 237–245

Contents lists available at ScienceDirect

Applied Catalysis B: Environmental

journal homepage: www.elsevier.com/locate/apcatb

Construction of ultrafine and stable PtFe nano-alloy with ultra-low Pt loading for complete removal of CO in PROX at room temperature

Hua Zhang [a], Xiaojuan Liu [a], Nuowei Zhang [a,*], Jinbao Zheng [a], Yanping Zheng [b], Yunhua Li [a], Chuan-Jian Zhong [c], Bing H. Chen [a,**]

[a] Department of Chemical and Biochemical Engineering, National Engineering Laboratory for Green Productions of Alcohols-Ethers-Esters, College of Chemistry and Chemical Engineering, Xiamen University, Xiamen 361005, China
[b] State Key Laboratory for Physical Chemistry of Solid Surfaces, Collaborative Innovation Center of Chemistry for Energy Materials, Department of Chemistry, College of Chemistry and Chemical Engineering, Xiamen University, Xiamen 361005, China
[c] Department of Chemistry, State University of New York at Binghamton, Binghamton, New York 13902, United States

ARTICLE INFO

Article history:
Received 17 March 2015
Received in revised form 21 May 2015
Accepted 16 June 2015
Available online 23 June 2015

Keywords:
Ultrafine PtFe alloy
Structure-activity relationship
Preferential oxidation of CO
Ultra-low Pt loading

ABSTRACT

Rational design of highly effective catalysts based on the understanding of structure–activity relationship is becoming more and more important in heterogeneous catalysis. In this study, we have designed and successfully prepared a highly active PtFe nano-alloy catalysts with ultra-low Pt loading for the preferential oxidation of CO, over which CO can be completely removed at room temperature. As compared to the previously reported Pt@Fe quasi-core–shell catalysts with similar performance, the Pt loading of the as-prepared $PtFe/Al_2O_3$ nano-alloy catalysts can be decreased by a factor of 6 due to the increased Pt utilization. Based on in situ diffuse reflectance infrared spectroscopy (DRIFTS) and quasi-in situ XPS, it can be concluded that O_2 is activated over ferrous iron on the $PtFe/Al_2O_3$ nano-alloy catalysts, leading to the high performance towards preferential oxidation of CO. Under reaction conditions, the active species will be oxidized to ferric oxide, thus O_2 activation ability and catalytic activity decrease. Based on the above understanding, we further constructed a highly stable catalyst by supporting PtFe nano-alloy particles onto TiO_2, which can help to activate O_2 and stabilize the lower valence Fe species.

1. Introduction

Due to the development of nano-technology and characterization techniques [1], tremendous progresses have been made in understanding the structure–activity relationship, thus the catalytic activity, selectivity and stability can be enhanced via scientific catalyst design based on these findings. For example, Henning et al. [2] maximized the activity for the oxidation of benzyl alcohol by precisely controlling the Pd shell thickness, inspired by the idea that Pd shell would remarkably promote the performance of PdAu bimetallic catalyst [3]. Kahsar et al. [4] and Kwon et al. [5] reported that the selectivity in several hydrogenation reactions could be tuned by changing adsorption energetics or configuration of reactant via surface modification of nanocatalysts with capping agent. Knowing sintering of nanoparticles at evaluated temperature would lead to deactivation, Lu et al. [6] and Joo et al. [7] then coated nanocatalysts with porous oxide layer to suppress the sintering process thus improved the long-term stability. These results not only discovered efficient catalysts for specific reactions, but also emphasized the importance of rational design of catalyst composition and structure according to the structure–activity relationship.

As for preferential oxidation of CO (PROX), which is of significant importance in both research and industrial application, several fundamental insights into the catalytic mechanism over supported metal catalysts have also been gained, such as the size and structure effects [8,9], support effects [10–13], interfacial effects [14], influence of water [15,16], identification of active sites [17–19] and intermediates [20–22], and discussion of reaction pathways [23–26]. Nowadays, it is well known that the oxidation of CO follows the Langmuir–Hinshelwood mechanism, and particular attention should be paid to the activation of O_2, which will be inhibited by the strong adsorption of CO on the catalyst surface. Guided by this idea, coordinately unsaturated transition metal oxide or hydroxide decorated Pt nanocatalysts have been prepared successfully, and their structure can be described as quasi-core–shell structure (Pt@Fe), where the core was dominated by Pt and transition metal located on the surface [27,28]. These catalysts are highly active towards the oxidation of CO, and conversion of CO can reach

* Corresponding author.
** Corresponding author. Fax: +86 5922184822.
E-mail addresses: zhnw@xmu.edu.cn (N. Zhang), chenbh@xmu.edu.cn (B.H. Chen).

http://dx.doi.org/10.1016/j.apcatb.2015.06.032
0926-3373/

100% even at room temperature. Our recent work demonstrated the promotional effect was originated from the efficient activation of O_2 by transition metal species according to the CO/O_2 pusle experiments, and the performance would increase with the oxophilicity of transition metal [29].

Considering the catalytic process occurs on the surface of catalysts and the catalytic property is mostly determined by the surface atoms, we believe that the established Pt@Fe quasi-core–shell catalysts may not be the most promising candidates for PROX. The cores of the metal nanoparticles are dominated by Pt in these catalysts, and only few Pt atoms are located on the surface and participate in the reaction, leading to the fairly low utilization of Pt. Thus, the loadings of Pt on these catalysts are very high, and the activity will decrease significantly if the loadings are lower than 1% [30]. Due to the high price of noble metal, this will greatly limit their industrial applications.

Inspired by these results, we try to design a more efficient catalyst for PROX with lower Pt loading, on which Fe is alloyed with Pt rather than decorating its surface. Therefore, the cores are diluted by Fe atoms and more Pt atoms will present on the catalyst surface, and the utilization of Pt can be enhanced. However, due to the remarkable difference between the redox potential of Pt and Fe, quasi-core–shell structure, where Fe enriched on the surface, rather than homogeneous alloy were usually obtained via co-reduction processes [29,31]. Though a few studies have succeeded in the direct synthesis of PtFe alloy particles through high temperature reduction [32] or decomposition [33], the particle size is usually as large as 5 nm. This would significantly decline the Pt utilization and the intrinsic activity [34]. On the whole, it still remains a great challenge to synthesize ultrafine PtFe alloy nanoparticles.

In this study, supported PtFe alloy nanoparticles with a Pt loading of only about 0.7% and size smaller than 2 nm has been successfully synthesized by carefully controlling the reduction conditions. This catalyst shows much higher reaction rate than other highly active Pt-based catalysts reported recently, and 100% CO conversion can be achieved even at room temperature. We found the pH value was crucial for the preparation of highly active catalysts, which would affect the catalyst composition, particle size and performance, and 100% CO conversion at room temperature could only be obtained when the pH was over 7. Based on the characterization results of X-ray diffraction (XRD), transmission electron microscopy (TEM), high angle annular dark field-scanning transmission electron microscopy-energy dispersive spectrometer (HAADF-STEM-EDS), high-sensitivity low-energy ions scattering (HS-LEIS), CO temperature programmed desorption (CO-TPD) and in situ diffuse reflectance infrared spectroscopy (DRIFTS), the structure of the bimetallic catalyst was confirmed as ultrafine PtFe alloy with particle size smaller than 2 nm, and its excellent performance was originated from the increased Pt utilization and the efficient activation of O_2 over Fe. These active species for O_2 activation were further identified as ferrous iron by quasi-in situ X-ray photoelectron spectroscopy (XPS). They would be oxidized into ferric iron during reaction, leading to deactivation. TiO_2, which can help to activate O_2 and stabilize the lower valence Fe species, was further used to support the PtFe alloy nanoparticles in order to obtain a robust catalyst for PROX. As expected, $PtFe/TiO_2$ was extremely stable for PROX, and no deactivation was observed during testing.

2. Experiment

2.1. Chemicals

γ-Al_2O_3 was purchased from Aluminum Corporation of China and calcinated at 500 °C for 4 h before being used. Carbon nanotube (CNT) was kindly provided by Professor Hongbin Zhang at Xiamen University and refluxed in HNO_3 for 12 h. It has been washed with distilled water and dried at 105 °C before use. TiO_2 (P25) was purchased from Degussa, and other chemicals, such as chloroplatinic acid, ferric chloride and ethylene glycol, were purchased from Sinopharm Chemical Reagent Co., and used as received.

2.2. Catalysts preparation

The catalysts were prepared by a one-pot surfactant-free polyol process. Typically, for the preparation of $Pt_{0.71}Fe_{0.23}/Al_2O_3$, 1000 mg γ-Al_2O_3 were dispersed in 100 mL ethylene glycol and treated with ultrasonic for 60 min to form a homogeneous slurry. Then, 2.65 mL H_2PtCl_6 ethylene glycol solution (3.8 mg Pt/mL) and 5.73 mL $FeCl_3$ ethylene glycol solution (7 mg Fe/mL) were added and stirred for 60 min. After adjusting the pH to 13 with 1 M NaOH solution (dissolved in ethylene glycol), the dispersion was refluxed under N_2 at 160 °C for 3.5 h. After cooling down to room temperature, the pH was adjusted to 2 with 1 M HCl solution (dissolved in deionized water), and the dispersion was stirred overnight. Finally, the slurry was filtered and washed thoroughly with deionized water and dried in a vacuum oven at 60 °C for 10 h. $Pt_{0.78}/Al_2O_3$ was prepared without the addition of $FeCl_3$. Similar procedures have also been conducted to prepare $Pt_{0.77}Fe_{0.23}$/CNT and $Pt_{0.77}Fe_{0.23}/TiO_2$, but 1000 mg CNT or TiO_2 were dispersed in ethylene glycol for the preparation of $Pt_{0.77}Fe_{0.23}$/CNT and $Pt_{0.77}Fe_{0.23}/TiO_2$, respectively. We also studied the influence of the starting pH value on the catalyst preparation and catalytic performance. For this study, the starting pH value was adjusted to 7, 5 and 4 to prepare $Pt_{0.71}Fe_{0.17}/Al_2O_3$, $Pt_{0.55}Fe_{0.07}/Al_2O_3$ and $Pt_{0.44}Fe_{0.02}/Al_2O_3$. All the catalysts were reduced at 500 °C under H_2 for 2 h before catalytic tests.

2.3. Characterization of the catalysts

The bulk composition of the samples was determined by inductively coupled plasma atomic emission spectroscopy (ICP-AES). TEM images and energy dispersive X-ray spectroscopy (EDS) for elemental mapping and line-scan analysis of the samples were obtained on Tecnai F30 with an accelerating voltage of 300 kV. The size distribution was determined by counting at least 200 particles. HS-LEIS analysis was carried out on an Ion-TOF Qtac100 low energy ion scattering analyzer and Ne^+ ions with a kinetic energy of 5 keV were applied.

CO-TPD experiments were conducted in a home-made setup equipped with mass spectrometry to analyse the composition of desorption gas. The catalysts were pre-treated at 500 °C for 5 h under H_2, which was identical to the pretreatment condition for PROX reaction. After cooling down to 50 °C, the feed gas was changed into CO (99.9%, 50 mL/min) for another 2 h. Then, He (99.999%, 30 mL/min) was used as carrier gas, and temperature was ramped from 50 °C to 500 °C at a speed of 10 °C/min. Composition of the desorption gas was analyzed by an on-line mass spectrometry. In order to eliminate the influence of CO_2 on CO signal, CO_2 in the desorption gas was removed by NaOH before mass spectrometry analysis.

In situ DRIFTS of $Pt_{0.72}/Al_2O_3$ and $Pt_{0.71}Fe_{0.23}/Al_2O_3$ was recorded on BRUKER VERTEX 70 equipped with a PIKE diffuse reflectance accessory and an in situ chamber. Before the DRIFTS measurements, about 15 mg catalyst were loaded into the chamber and reduced under H_2 at 500 °C for 2 h. After cooling down to 20 °C, the chamber was evacuated for 30 min, and the spectrum of the catalyst was recorded and used as background for following measurements. 1.0 kPa CO was then introduced to the chamber. After equilibrating for 10 min, the infrared (IR) spectrum was recorded. Then different pressure of O_2 was introduced, and the IR spectrum was recorded under each pressure. All the results described

here were obtained by averaging 64 scans in each spectrum with a spectral resolution of 4 cm^{-1}.

Quasi in situ X-ray photoelectron spectroscopy (quasi-in situ XPS) measurements were carried out with a VG MultiLab 2000 spectrometer with an Omicron Sphera II hemispherical electron energy analyser and a home-made reaction chamber. Monochromatic Al Kα X-ray source (1486.6 eV, anode operating at 15 kV and 300 W) was used to excite XPS spectra. The constant pass energy is 40 eV, and the base pressure of the system was 5.0×10^{-9} mbar. The binding energies in all the spectra were calibrated according to C 1s peak at 284.6 eV. As nano-sized Pt and Fe can easily be oxidized under air, actual information of the catalysts during reaction can hardly be obtained by traditional XPS. In our study, the catalysts were treated in the reaction chamber, and then transferred to the XPS analysis chamber through a load-lock gate without exposure to air. Thus, oxidation of the treated catalysts by air could be avoided. The catalysts were firstly treated under hydrogen at 500 °C for 2 h, and then transferred to the analysis chamber for XPS test. The recorded spectra were labelled as 500 °C reduction. The catalysts were then transferred to the reaction chamber again, and treated under 1% CO, 1% O_2, 50% H_2 and N_2 balance at room temperature for 5 h before the second XPS test. The resulted XPS spectra this time was labelled as PROX-5 h. It can be known that the spectra of 500 °C reduction and PROX-5 h represent the results of reduced and spent catalysts respectively, and the active sites and deactivation reason can be concluded from the difference of these two spectra. XPS spectra of Fe foil were also measured as reference. Due to the oxidation of Fe foil surface under atmosphere, XPS spectra of different Fe oxidation states can be obtained by controlling the sampling depth via Ar^+ sputtering. The surface of Fe foil was sputtered by Ar^+ ion with a kinetic energy of 8 keV and a current of 100 nA. The sputtering continued for 10 min and 20 min, in order to achieve a sputtering depth of about 3.2 nm and 6.4 nm, respectively.

2.4. Preferential oxidation of CO

Preferential oxidation of CO experiments were performed in a fixed-bed lab reactor at atmospheric pressure. In general, 50 mg catalyst were placed between quartz glass wools in a quartz reactor. The reaction mixtures consisted of 1% CO, 1% O_2, 50% H_2 and N_2 balance, and the total gas flow rate was 16.7 mL/min. The weight hourly space velocity (WHSV) was 20,000 mL g^{-1} h^{-1}, which corresponded to a gas hourly space velocity (GHSV) of about 70,000 h^{-1}. For the comparison of the activities of the samples prepared under different pH value, only 25 mg catalyst were loaded into the reactor, leading to a higher WHSV of 40,000 mL g^{-1} h^{-1}. The CO and O_2 conversions, and selectivity towards O_2 were defined as:

$$C_{CO} = \left(\frac{[CO]^0 - [CO]}{[CO]^0}\right) \times 100\%$$

$$C_{O_2} = \left(\frac{[O_2]^0 - [O_2]}{[O_2]^0}\right) \times 100\%$$

$$S_{O_2} = \frac{C_{CO}}{C_{O_2}} \cdots\cdots\cdots [O_2]^0 = 0.5\%$$

$$S_{O_2} = \frac{C_{CO}}{1.2 \times C_{O_2}} \cdots\cdots\cdots [O_2]^0 = 0.6\%$$

$$S_{O_2} = \frac{C_{CO}}{2 \times C_{O_2}} \cdots\cdots\cdots [O_2]^0 = 1.0\%$$

where [CO] and [O_2] are the concentrations at reactor exit, while $[CO]^0$ and $[O_2]^0$ represent feed concentrations, which were all measured by a chromatograph equipped with a TCD detector.

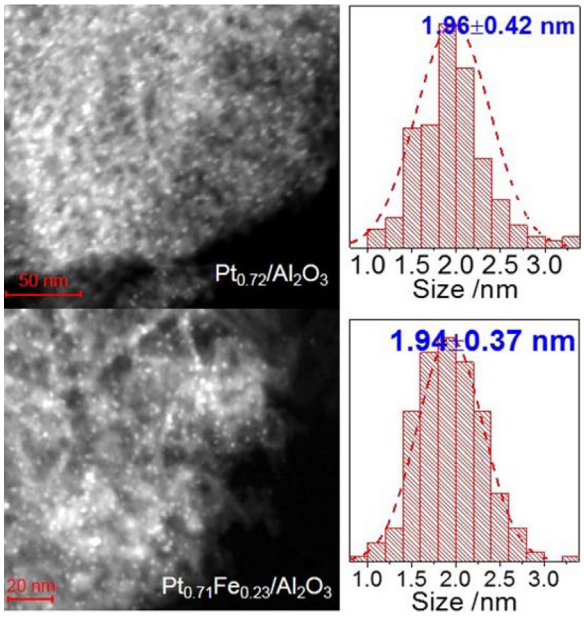

Fig. 1. HADDF-STEM images of $Pt_{0.72}/Al_2O_3$ and $Pt_{0.71}Fe_{0.23}/Al_2O_3$.

3. Results and discussion

3.1. Synthesis and characterization of PtFe bimetallic catalysts

In this study, $Pt_{0.72}/Al_2O_3$ and $Pt_{0.71}Fe_{0.23}/Al_2O_3$ were prepared via modified ethylene glycol reduction method under the pH of 13, 160 °C. The exact loadings of Pt on the catalysts determined by ICP for $Pt_{0.72}/Al_2O_3$ and $Pt_{0.71}Fe_{0.23}/Al_2O_3$ are 0.72 and 0.71 wt%, respectively, and the loadings of Fe are zero and 0.23%, respectively. As shown in Fig. 1 by STEM, the metal nanoparticles of both catalysts are highly dispersed on the catalyst surface, and their sizes are both around 1.9 nm. No diffraction peak assigned to the metal nanoparticles can be observed in the XRD results as shown in Fig. S1. This further illustrates that the size of the metal particles is very small. Therefore, it can be concluded that the Pt loading and particle size of both catalyst are the same within the uncertainty of the measurements.

Energy dispersive X-ray spectroscopy (EDS) for elemental mapping and line-scan analysis were conducted to study the fine structure of $Pt_{0.71}Fe_{0.23}$ nanoparticles. In order to reduce the impact of support and get better resolution during the EDS analysis, $Pt_{0.71}Fe_{0.23}$ nanoparticles were supported on less electron-dense CNT by the same synthesis strategy. As shown in Fig. S2, the particle size of $Pt_{0.71}Fe_{0.23}$ nanoparticles supported on CNT is similar to that on Al_2O_3, and their catalytic properties are also similar, which will be discussed in Section 3.2.

Fig. 2 shows the elemental mapping of $Pt_{0.71}Fe_{0.23}$ nanoparticles. It allows us to determine the distribution of Pt and Fe. The Pt signal matches well with the metal nanoparticles and Pt almost locates on every single nanoparticle. As both the loading and sensitivity factor of Fe are lower than Pt, it showed much weaker signal, leading to lower signal to noise ratio. Most of the light yellow areas are attributed to the noise, as no metal nanoparticles can be observed at these areas in the STEM image. As for the areas marked by white circles in Fig. 2, the color is deeper, which indicates Fe species are located at these areas. After overlapping the Fe and Pt mapping images, it can be observed these areas matches well with the signals of Pt. This means Pt and Fe are located very closely on the catalysts. The line-scan analysis for a single nanoparticle, as presented in Fig. 3, was further conducted in order to reveal the fine structure of the bimetallic catalysts. For the both place, a1 and a2, Pt trace

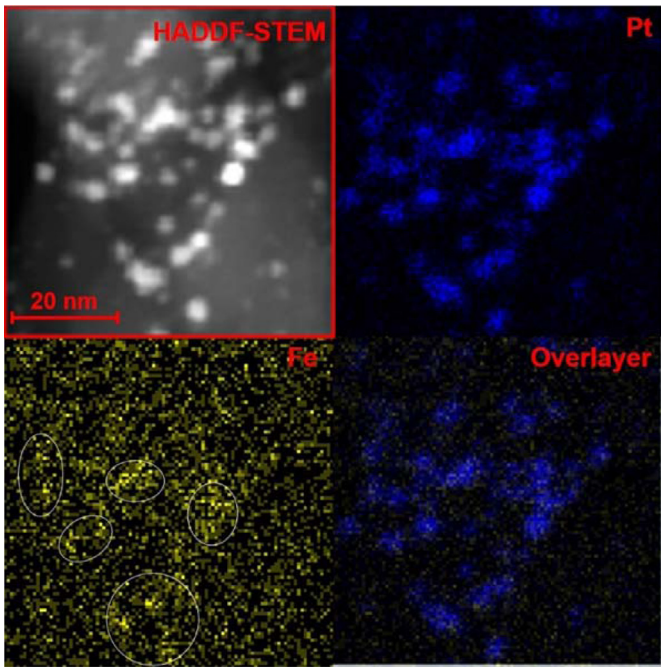

Fig. 2. HADDF-STEM images of $Pt_{0.71}Fe_{0.23}$ bimetallic nanoparticles supported on CNT and the corresponding elemental mapping results.

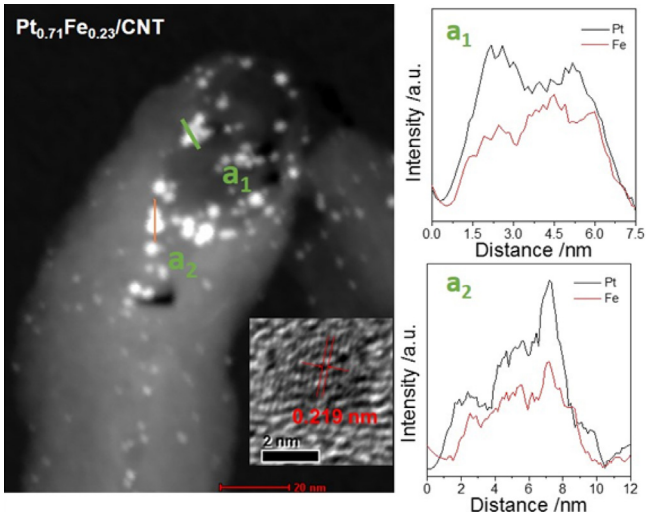

Fig. 3. Line-scan analysis of $Pt_{0.71}Fe_{0.23}$/CNT and the HRTEM image of a single nanoparticle (inset).

and Fe trace ascend then descend simultaneously, and the position of their peaks are almost identical. This suggests the bimetallic nanoparticles are presented as alloy structure. The inset in Fig. 3 shows a typical HRTEM image of the bimetallic nanoparticle. As can be seen, the interplanar spacing value is about 0.219 nm, which is slightly smaller than that of Pt(1 1 1) [35]. This further demonstrates the alloy structure between Pt and Fe.

Because the information from TEM only reflects the local region, we also studied the structure of $Pt_{0.71}Fe_{0.23}$ bimetallic nanoparticles by HS-LEIS, which could provide average information for the entire sample. HS-LEIS can not only give exclusive information on the outermost surface layer, but also help to uncover the subsurface structure of heterogeneous catalysts by increasing the ion current and sputtering time [36]. Fig. 4 shows the HS-LEIS analysis results of $Pt_{0.72}/Al_2O_3$ and $Pt_{0.71}Fe_{0.23}/Al_2O_3$. The signals of Fe and Pt are located at about 1.2 keV and 3.3 keV, respectively. Both of Pt and Fe signals can be observed on the first spectrum of $Pt_{0.71}Fe_{0.23}/Al_2O_3$, while only Pt signal on that of $Pt_{0.72}/Al_2O_3$. This indicates both Fe and Pt are exposed on the outermost surface of $Pt_{0.71}Fe_{0.23}/Al_2O_3$. With increasing sputter cycles, the two signals are still present on all the spectra of $Pt_{0.71}Fe_{0.23}/Al_2O_3$. This is very different with our previous HS-LEIS results of Pt@Fe quasi-core–shell catalysts, where Fe signal can be only observed on the first spectrum [29]. As well known, the surface of catalysts would be sputtered by the Ne^+ ions, and the sampling depth would increase with increasing sputter cycles. This means Pt and Fe coexist not only on the surface but also in the bulk of the bimetallic nanoparticles, and further confirms the homogeneous alloy structure between Fe and Pt. Possessing this alloy structure, the cores of the bimetallic nanoparticles are diluted by Fe atoms and more Pt atoms are presented on the surface, thus the utilization of Pt is increased as compared with Pt@Fe quasi-core–shell structue [27–29].

As it has been reported that pH value is crucial for the synthesis of monometallic catalysts [37,38], its influence on the preparation of PtFe bimetallic nano-alloy catalysts was also studied here. As shown in Fig. S3, the particle size of the bimetallic nano-alloy will increase from 1.9 nm to 3.6 nm when the pH value decreases from 13 to 4. This should be caused by the variation of glycolate concentration with the pH value, which is believed to be the stabilizer for colloids by forming chelate-type complexes via its carboxyl groups [39]. Furthermore, composition of the catalysts will also be affected by the pH value. As shown in Table S1, the Fe loading, Pt loading, and Fe/Pt mole ratio all decrease significantly with the decrease of pH value. This results indicate properties of PtFe nano-alloy catalyst are sensitive to the pH value, and the size and composition can be tuned via manipulating the pH value carefully.

3.2. Activity of PtFe bimetallic nano-alloy catalysts towards PROX and their structure–activity relationship

As indicated by the above characterization results, ultrafine PtFe alloy particles were obtained in this study. The catalytic properties of $Pt_{0.72}/Al_2O_3$ and $Pt_{0.71}Fe_{0.23}/Al_2O_3$ towards PROX were then studied at temperature from 25 °C to 200 °C, and the results were shown in Fig. 5. Similar with previous reports [40], the monometallic $Pt_{0.72}/Al_2O_3$ was quite inert for PROX at low temperature, due to the strong adsorption of CO on Pt surface, and the conversions of CO and O_2 were only about 20% at 100 °C. However, $Pt_{0.71}Fe_{0.23}/Al_2O_3$ was much more active than $Pt_{0.72}/Al_2O_3$, and both O_2 and CO can be completely converted even at room temperature. The conversion of O_2 maintained 100% while CO conversion declined slightly, as reaction temperature increased. This is because of the decreased selectivity at higher temperature, leading to part of O_2 reacting with H_2 [41]. As $Pt_{0.71}Fe_{0.23}$/CNT was used to reveal the bimetallic catalyst structure, its catalytic performance has also been studied and presented in Fig. S4, and similar results could be observed. As compared with the reported PtFe bimetallic catalysts with Pt@Fe quasi-core–shell structure and similar Pt loading [30], over which the conversion of CO at room temperature under similar conditions is only about 60%, the activity of the nano-alloy $Pt_{0.71}Fe_{0.23}/Al_2O_3$ in this study is much higher. This means the catalyst structure is essential for its catalytic performance, and the utilization of Pt and activity can be remarkably improved via changing the structure from Pt@Fe quasi-core–shell to nano-alloy. We have also compared the reaction rate of our nano-alloy catalysts with other highly active bimetallic Pt-based catalysts, such as PtCu intermetallic compound [42], Pt-Co/YSZ [43], Fe^{3+}-OH-Pt [27] and Pt@FeO/SiO_2 [28]. As shown in Table S2, most of the reaction rate of reported Pt-based nanocatalysts are smaller than 3×10^{-2} mol g_{Pt}^{-1} s^{-1} except that of trimetallic Cu@Pt-Fe catalysts, which is about 3.67×10^{-2} mol g_{Pt}^{-1} s^{-1}. The PtFe nanoalloy catalyst reported in this work shows much higher rate, which is about

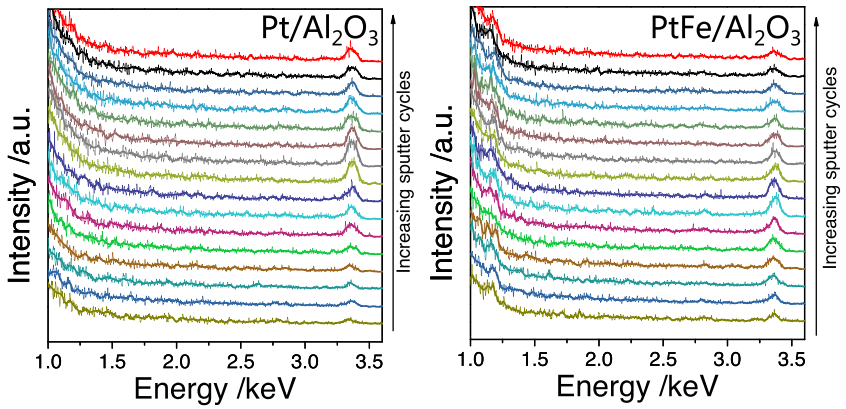

Fig. 4. HS-LEIS spectrums of $Pt_{0.72}/Al_2O_3$ and $Pt_{0.71}Fe_{0.23}/Al_2O_3$.

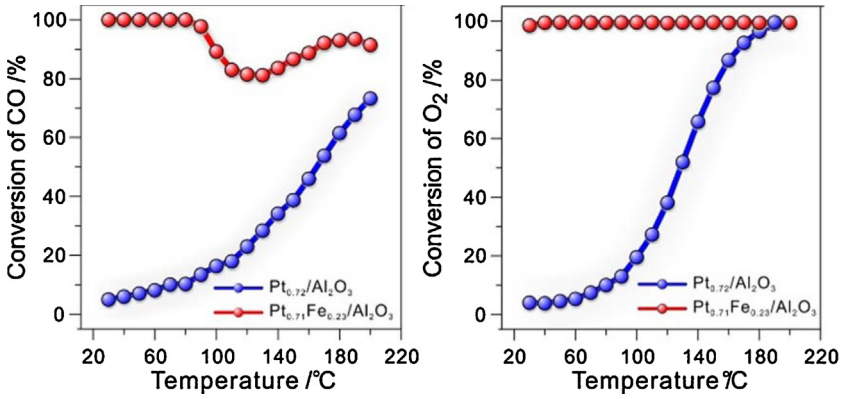

Fig. 5. Catalytic results of $Pt_{0.72}/Al_2O_3$ and $Pt_{0.71}Fe_{0.23}/Al_2O_3$ for PROX.
Left: conversion of CO; Right: conversion of O_2.
Reaction conditions: 1% CO, 1% O_2, 50% H_2, N_2 balance, GHSV of 20,000 mL/(h g). As shown in Fig. S5 in the supporting information, the conversion of CO at 30 °C is 100% even at a GHSV of 40,000 mL/(h g).

6.28×10^{-2} mol g_{Pt}^{-1} s^{-1}. Thus, we believe that the PtFe nanoalloy is a highly active catalyst in PROX.

As discussed above, the size and composition of the PtFe nanoalloy will be effected by the pH value during the preparation process. Thus, we further studied the influence of the pH value on the catalytic performance. As shown in Fig. S5, the activity decreases distinctly with the decrease in the pH value, due to the increase of particle size and the decrease of Fe and Pt loading. The conversion for $Pt_{0.71}Fe_{0.23}/Al_2O_3$ prepared under pH 13 can reach 100% at room temperature, while almost no CO can be converted over $Pt_{0.44}Fe_{0.02}/Al_2O_3$ prepared under pH 5 at the same condition. This result illustrates the catalytic performance of PtFe nano-alloy catalysts will be significantly affected by the pH value during catalysts preparation, and particular attention should be paid to control it in order to maximize the activity.

In order to reveal the role of Fe towards PROX, we further studied $Pt_{0.72}/Al_2O_3$ and $Pt_{0.71}Fe_{0.23}/Al_2O_3$ by CO-TPD and in situ DRIFTS. As the low activity of Pt/Al_2O_3 is originated from the strong adsorption of CO on the Pt surface, it is reasonable to speculate that Fe may weaken the adsorption strength of CO and then lead to the enhanced performance. CO-TPD is one of the most frequently used method to monitor the CO adsorption strength [44]. The temperature of desorption peaks represents qualitatively the strength of CO binding sites, and it will increase with the increase in adsorption strength [45]. We firstly studied the catalysts by CO-TPD, and the results are shown in Fig. 6. The CO desorption peak of $Pt_{0.72}/Al_2O_3$ is located at about 200 °C, while that of $Pt_{0.71}Fe_{0.23}/Al_2O_3$ at 225 °C. This indicates that Fe species will increase the CO adsorption strength, which obviously cannot explain the high activity of $Pt_{0.71}Fe_{0.23}/Al_2O_3$. It can be also observed that large amount of CO_2 were desorbed from the catalyst surface between 100 °C and 550 °C (not shown here), if NaOH was not used to purify the desorption gas before mass spectrometry analysis. This indicates CO can react with OH groups present on the support surface via the water gas shift reaction (WGSR) [46]. The CO-TPD of after PROX are also shown in Fig. 6, which will be discussed later.

As in situ IR method allows to study the adsorption state of surface intermediates, we then tried to uncover the promotional effects of Fe by in situ DRIFTS. Before the measurements, both of $Pt_{0.72}/Al_2O_3$ and $Pt_{0.71}Fe_{0.23}/Al_2O_3$ were reduced at 500 °C for

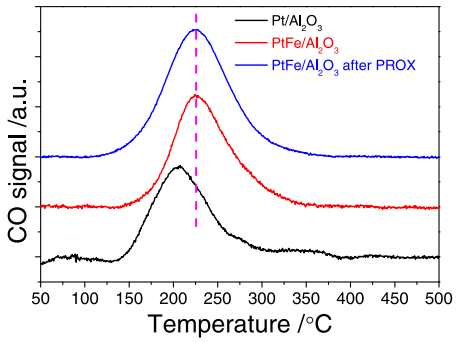

Fig. 6. CO-TPD results of $Pt_{0.72}/Al_2O_3$ and $Pt_{0.71}Fe_{0.23}/Al_2O_3$.

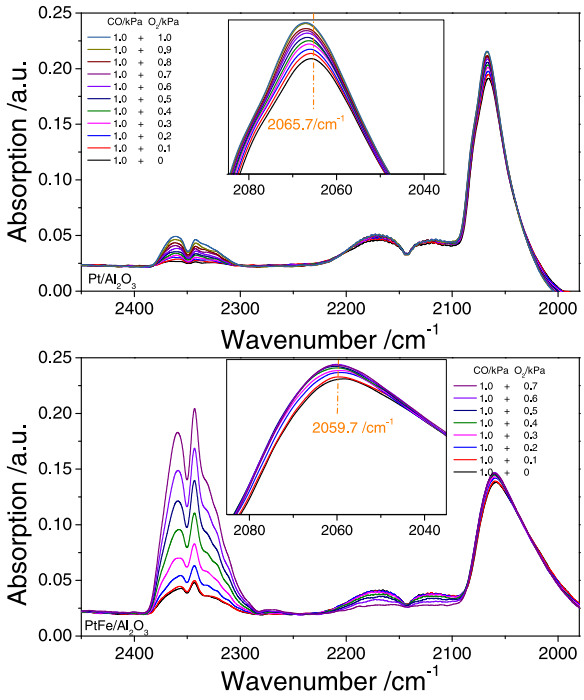

Fig. 7. In situ DRIFTS study on the co-adsorption of CO and O_2 on $Pt_{0.72}/Al_2O_3$ and $Pt_{0.71}Fe_{0.23}/Al_2O_3$.

2 h then cooled down to room temperature. After evaluation for 30 min, the spectra of the catalysts under vacuum were collected and used as background for the subsequent measurements. During the test, 1.0 kPa CO was firstly introduced to the system, and the corresponding spectra were recorded. Then, different pressure of O_2 was introduced to study the co-adsorption of CO and O_2 on the catalysts surface. As shown in Fig. 7, for both catalysts, there are three sets of peaks located at 2400–2250 cm^{-1}, 2220–2150 cm^{-1} and 2100–2000 cm^{-1}, corresponding to gas phase CO_2, CO and linearly adsorbed CO, respectively [47]. It can be observed from the insets of Fig. 7 that addition of Fe to Pt/Al_2O_3 will lead to a red shift of the linear adsorbed CO signals. It's located at 2065.7 cm^{-1} for $Pt_{0.72}/Al_2O_3$, while at 2059.7 cm^{-1} for $Pt_{0.71}Fe_{0.23}/Al_2O_3$. This means the adsorption strength may be different in this two samples. The red shift of linear adsorbed CO signal for $Pt_{0.71}Fe_{0.23}/Al_2O_3$ indicates more back-donation of electrons from Pt to the 2p anti-bonding orbital of CO, i.e., the interactions between Pt and CO get increased. This is well consistent with the above CO-TPD results, which also demonstrate the stronger adsorption of CO on $Pt_{0.71}Fe_{0.23}/Al_2O_3$ than on $Pt_{0.72}/Al_2O_3$. Gas phase CO_2 can be produced even in the absence of O_2, which should result from the reaction between CO and surface hydroxyl groups via WGSR [48]. After the introduction of O_2, the intensity of CO_2 rises significantly. It can be seen that the intensity of CO_2 for $Pt_{0.71}Fe_{0.23}/Al_2O_3$ is much higher and rises much more rapidly with increased O_2 pressure as compared with that for $Pt_{0.72}/Al_2O_3$. This indicates a higher activity of $Pt_{0.71}Fe_{0.23}/Al_2O_3$, which is consist with the activity results for PROX. At the same time, it can be seen that the intensity of linear adsorbed CO was almost stable, while the intensity of gas CO decreased rapidly. This means CO can be adsorbed on Pt surface as long as the uncovered Pt surface is exposed due to the surface reactions between absorbed oxygen and CO.

Although the adsorbed oxygen species are difficult to be distinguished directly from IR spectrum due to the strong absorption of IR light below 1000 cm^{-1} by the support, it can be speculated indirectly from the position of the peak of linear adsorbed CO. The insets in Fig. 7 magnified the regions of linearly adsorbed CO and showed the influence of O_2 pressure on the peak position of linear adsorbed CO. Similar with previous reports [49,50], remarkable blue shift can be observed for the peak of linearly adsorbed CO on $Pt_{0.72}/Al_2O_3$ with increase of O_2 pressure, which reflects the decreased back-donation of electrons from Pt to the 2p anti-bonding orbital of CO [51,52]. This indicates the co-adsorption of oxygen and CO on the Pt surface, by which the electron density of Pt is reduced due to the electron-withdrawing effect of oxygen, leading to the less back-donation of electrons [53]. However, the peak location of linearly adsorbed CO on $Pt_{0.71}Fe_{0.23}/Al_2O_3$ is constant, when the oxygen pressure increases from 0 kPa to 1.0 kPa. This means the electron density of Pt on $Pt_{0.71}Fe_{0.23}/Al_2O_3$ is not altered by the adsorption of O_2, which further indicates that O_2 is absorbed on Fe rather than Pt.

The in situ DRIFTS results show both CO and O_2 are adsorbed competitively on Pt surface for $Pt_{0.72}/Al_2O_3$, while CO on Pt and O_2 on Fe for $Pt_{0.71}Fe_{0.23}/Al_2O_3$. Considering the strong binding of CO, all the Pt surface will be covered by CO when exposed to CO + O_2, which will inhibit the activation of O_2. Thus, $Pt_{0.72}/Al_2O_3$ is quite inert at low temperature. However, as for $Pt_{0.71}Fe_{0.23}/Al_2O_3$, O_2 can still be activated on Fe to form active oxygen species, such as O_2^- or O_2^{2-}, even when all the Pt surface is occupied by CO. Then the active oxygen species further react with the adsorbed CO at the perimeter between Pt and Fe, leading to the outstanding catalytic performance of $Pt_{0.71}Fe_{0.23}/Al_2O_3$. This mechanism is consistent with our previous results of pulse experiment [29] and can also be proved by DFT calculations [27,28].

3.3. Stability of the PtFe bimetallic nano-alloy catalysts

As well known, the stability is of significant importance in heterogeneous catalysis, especially for the studies involved in industrializations. Herein, we also studied the stability of the PtFe bimetallic nano-alloy catalysts. As shown in Fig. 8a and b, distinct deactivation of $Pt_{0.71}Fe_{0.23}/Al_2O_3$ can be observed at 30 °C. While increasing the oxygen partial pressure, the deactivation rate gets faster. As reported by Liu et al. [54], two reasons may lead to the deactivation of Pt-based catalysts. One is the poisoning of Pt by CO, the other is the oxidation of catalysts by O_2. Thus, we further studied the exact deactivation reason for the PtFe nanoalloy catalysts by pre-treating the catalysts with CO or O_2 at room temperature before reactions. As shown in Fig. 8c and d, the sample pre-treated under CO showed a very similar catalytic results to the untreated catalyst. Much lower activity was observed for the sample pre-treated under O_2. Its initial CO conversion was only about 25%, and it would decrease to 15% after reaction for 300 min. According to these results, it can be speculated that the loss of activity results from the oxidation of Pt or/and Fe on the catalysts by O_2, rather than the poisoning of Pt by CO.

We further studied the catalysts by XPS to reveal their structure changes during reaction and the active species for PROX. The XPS measurements were performed under quasi-in situ conditions, as nano-sized Pt and Fe can be easily oxidized under air and thus actual information of the catalysts can hardly be obtained by traditional XPS. During the quasi-in situ XPS experiment, exposure of the catalyst to air can be avoid. The catalyst was treated in a reaction chamber and then transferred through a load-lock gate to analysis chamber after evacuating the reaction chamber to the 10^{-6} Pa range to record the XPS data. Fig. 9 shows the XPS data of $Pt_{0.71}Fe_{0.23}/Al_2O_3$ after reduction and PROX reaction. The signals of Pt $4d_{3/2}$ and Pt $4d_{5/2}$ are located at 314.6 eV and 331.5 eV, respectively, which are typical values for metallic Pt [55–57]. They are almost constant regardless of the treatment conditions. This indicates the state of Pt species on the reduced catalyst and spent catalyst is identical and it can maintain metallic state even after

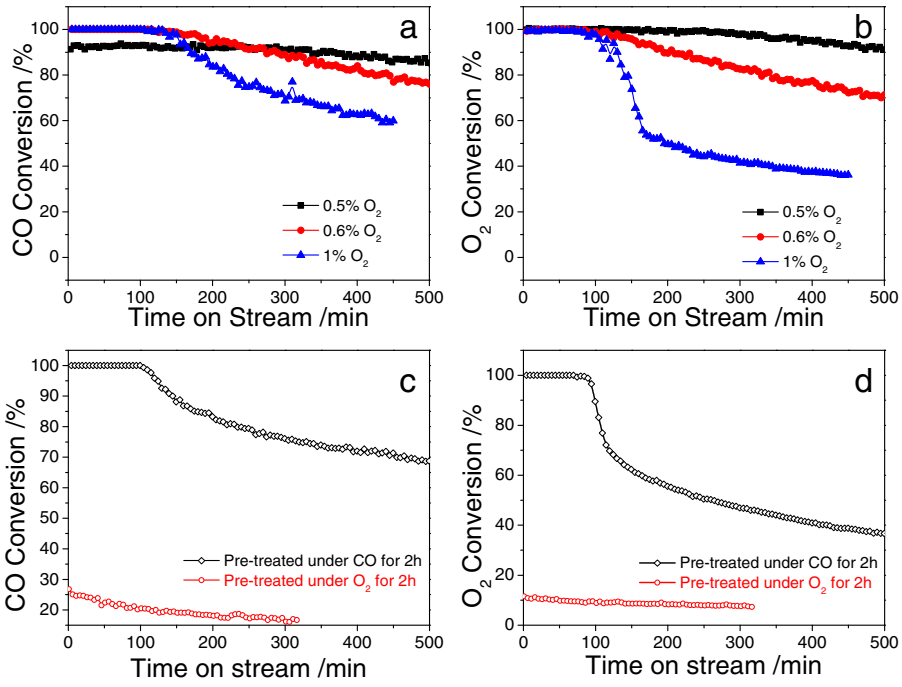

Fig. 8. Time on stream of $Pt_{0.71}Fe_{0.23}/Al_2O_3$ for PROX at room temperature.
(a,b): Effect of O_2 concentration in feed gas on the stability of $Pt_{0.71}Fe_{0.23}/Al_2O_3$. The legends define the O_2 concentration during reaction. (c,d): Effect of pretreatment condition on the on the stability of $Pt_{0.71}Fe_{0.23}/Al_2O$, when O_2 concentration in feed gas is 1%.
Reaction conditions: 30 °C, 1% CO, 50% H_2, N_2 balance, GHSV of 20,000 mL/(h g).

PROX reaction. Thus, it can be concluded that the deactivation is not caused by the oxidation of Pt.

The 500 °C reduction one represents $Pt_{0.71}Fe_{0.23}/Al_2O_3$ reduced under H_2 at 500 °C for 2 h, and the PROX-5 h one represents $Pt_{0.71}Fe_{0.23}/Al_2O_3$ further exposed to PROX reaction for 5 h at 30 °C after 500 °C reduction.

Due to the complexity of Fe, XPS of Fe foil was firstly measured as a reference. It is well known that the surface of Fe foil will be oxidized under atmosphere while the bulk still maintain metallic form, i.e., the degree of oxidation decreases with the increase of depth. Thus, XPS spectra of different Fe oxidation states can be obtained by controlling the sampling depth via Ar^+ sputtering. As shown in Fig. 9b, there is only one $2p_{3/2}$ peak located at 711.5 eV on fresh Fe foil, which can be ascribed to Fe^{3+} [58,59]. Another two peaks can be observed after Ar^+ sputtering, and the intensity will increase with sputtering time due to surface cleaning. These two peaks are located at 710.4 eV and 707.2 eV, which can be ascribed to Fe^{2+} and Fe^0, respectively [60–62]. Based on these results, we then studied the variation of Fe oxidation states during reaction. The Fe $2p_{3/2}$ peak of $Pt_{0.71}Fe_{0.23}/Al_2O_3$ after reduction located at 710.4 eV, which means the Fe species are presented as Fe^{2+}. However, for $Pt_{0.71}Fe_{0.23}/Al_2O_3$ after PROX-reaction, the binding energy of Fe $2p_{3/2}$ is shifted to about 711.5 eV, indicating the presence of Fe^{3+}. This means Fe^{2+} will be oxidized to Fe^{3+} during PROX reaction. As shown in the CO-TPD results of Fig. 6, the desorption signal for $Pt_{0.71}Fe_{0.23}/Al_2O_3$ after PROX reaction arises at about 225 °C, which is the same as the fresh sample. This means the oxidation of Fe species during RPOX reaction won't affect the adsorption strength of CO. As reported previously [63], Fe^{2+} are the active site for the activation of oxygen, while it is hard for Fe^{3+} to activate O_2. Thus, it can be concluded that the oxidation of Fe^{2+} to Fe^{3+} decreases the ability of O_2 activation, and thus leads to the loss of activity during PROX reaction.

Based on the above discussion, increasing the O_2 activation ability and the stability of low valence Fe species is of significance to obtain a stable PtFe bimetallic catalyst. Due to the abundant

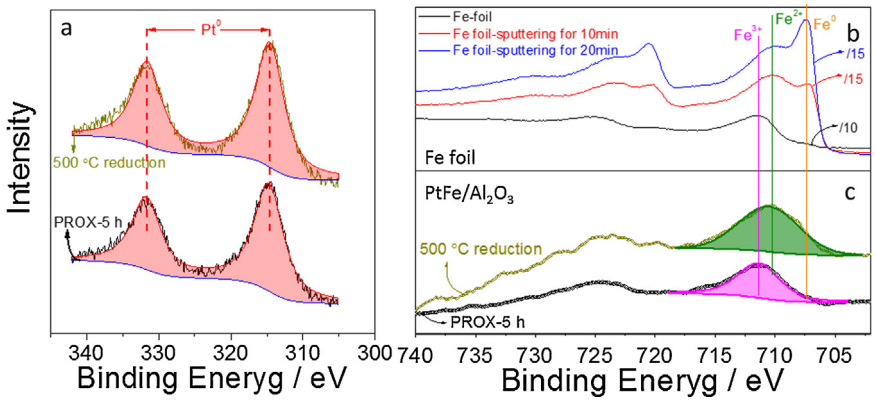

Fig. 9. Quasi-in situ XPS data of $Pt_{0.71}Fe_{0.23}/Al_2O_3$ treated under different conditions. (a) Pt 4d; (b) Fe 2p of Fe foil; (c) Fe 2p of $Pt_{0.71}Fe_{0.23}/Al_2O_3$.

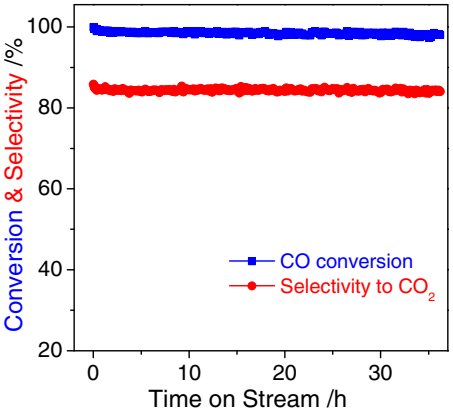

Fig. 10. Time on stream of $Pt_{0.71}Fe_{0.23}/TiO_2$ towards PROX. Reaction conditions: 30 °C, 1% CO, 0.6% O_2, 50% H_2, N_2 balance, GHSV of 20,000 mL/(h g).

defects on the surface, TiO_2 is much more active in activation of O_2 than Al_2O_3 [64–66]. Furthermore, oxygen vacancy and Ti^{3+} on its surface are able to act as electron donors [67], helping to reduce and stabilize the metal nanoparticles via strong metal-support interaction [68,69]. Thus, we then supported bimetallic $Pt_{0.71}Fe_{0.23}$ nano-alloy onto TiO_2 via similar method and studied its performance towards PROX. The result is presented in Fig. 10. As expected, $Pt_{0.71}Fe_{0.23}/TiO_2$ is much more stable than $Pt_{0.71}Fe_{0.23}/Al_2O_3$, and no activity loss can be observed during the test.

4. Conclusions

In this study, we constructed ultrafine PtFe bimetallic nano-alloy catalysts via polyol method to increase the utilization of Pt. The alloy structure of PtFe bimetallic nanoparticles was unambiguously proved by elemental mapping, line-scan analysis and HS-LEIS. As compared with previously reported PtFe catalysts, which possessed a structure of Fe rich surface and Pt dominated core, the as-prepared PtFe nano-alloy catalysts are much more active and the Pt loading can be decreased by a factor of 6. The reaction mechanism of PROX over $Pt_{0.72}/Al_2O_3$ and $Pt_{0.71}Fe_{0.23}/Al_2O_3$ were also studied by in situ DRIFTS and Quasi-in situ XPS. By in situ DRIFTS, it was directly observed that the adsorption of CO and O_2 proceeded on Pt and Fe respectively for $Pt_{0.71}Fe_{0.23}/Al_2O_3$, while competitively on Pt for $Pt_{0.72}/Al_2O_3$. Thus, the promotional effects of Fe can be ascribed to the efficient activation of O_2 on Fe species, even though Pt surface is completely covered by CO. The active Fe species for O_2 activation were further identified as Fe^{2+} by quasi-in situ XPS. Under PROX condition, these species will be oxidized to Fe^{3+}, which is incapable of activating O_2, leading to the deactivation of $Pt_{0.71}Fe_{0.23}/Al_2O_3$ towards PROX. Guided by these results, we then constructed a highly stable catalyst by supported PtFe nano-alloy particles onto TiO_2, which is active for the activation of O_2 and can stabilize the lower valence Fe species. This study presents a case in how to design more efficient and cheaper catalyst by understanding the intrinsic catalytic behavior and the structure–activity relationship, and we believe the findings in our study will play important roles in deepening the mechanistic insight for not only PROX but also other oxidation reactions and will also help to design new catalysts in a more scientific way.

Acknowledgement

This work was supported by the National Natural Science Foundation of China (Grant Nos. 21303140 and 21336009).

Appendix A. Supplementary data

Supplementary data associated with this article can be found, in the online version, at http://dx.doi.org/10.1016/j.apcatb.2015.06.032

References

[1] G.A. Somorjai, H. Frei, J.Y. Park, J. Am. Chem. Soc. 131 (2009) 16589–16605.
[2] A.M. Henning, J. Watt, P.J. Miedziak, S. Cheong, M. Santonastaso, M.H. Song, Y. Takeda, A.I. Kirkland, S.H. Taylor, R.D. Tilley, Angew. Chem. Int. Ed. 52 (2013) 1477–1480.
[3] D.I. Enache, J.K. Edwards, P. Landon, B. Solsona-Espriu, A.F. Carley, A.A. Herzing, M. Watanabe, C.J. Kiely, D.W. Knight, G.J. Hutchings, Science 311 (2006) 362–365.
[4] K.R. Kahsar, D.K. Schwartz, J.W. Medlin, J. Am. Chem. Soc. 136 (2013) 520–526.
[5] S.G. Kwon, G. Krylova, A. Sumer, M.M. Schwartz, E.E. Bunel, C.L. Marshall, S. Chattopadhyay, B. Lee, J. Jellinek, E.V. Shevchenko, Nano Lett. 12 (2012) 5382–5388.
[6] J. Lu, B. Fu, M.C. Kung, G. Xiao, J.W. Elam, H.H. Kung, P.C. Stair, Science 335 (2012) 1205–1208.
[7] S.H. Joo, J.Y. Park, C.-K. Tsung, Y. Yamada, P. Yang, G.A. Somorjai, Nat. Mater. 8 (2009) 126–131.
[8] M. Valden, X. Lai, D.W. Goodman, Science 281 (1998) 1647–1650.
[9] M.S. Chen, D.W. Goodman, Science 306 (2004) 252–255.
[10] S. Li, H. Zhu, Z. Qin, G. Wang, Y. Zhang, Z. Wu, Z. Li, G. Chen, W. Dong, Z. Wu, L. Zheng, J. Zhang, T. Hu, J. Wang, Appl. Catal. B-Environ. 144 (2014) 498–506.
[11] O.H. Laguna, A. Pérez, M.A. Centeno, J.A. Odriozola, Appl. Catal. B-Environ. 176–177 (2015) 385–395.
[12] P. Sudarsanam, B. Mallesham, P.S. Reddy, D. Großmann, W. Grünert, B.M. Reddy, Appl. Catal. B-Environ. 144 (2014) 900–908.
[13] K. Yang, K. Huang, Z. He, X. Chen, X. Fu, W. Dai, Appl. Catal. B-Environ. 158–159 (2014) 250–257.
[14] Y. Bai, W. Zhang, Z. Zhang, J. Zhou, X. Wang, C. Wang, W. Huang, J. Jiang, Y. Xiong, J. Am. Chem. Soc. 136 (2014) 14650–14653.
[15] G. Li, L. Li, Y. Yuan, J. Shi, Y. Yuan, Y. Li, W. Zhao, J. Shi, Appl. Catal. B-Environ. 158–159 (2014) 341–347.
[16] O. Mihai, A. Fathali, X. Auvray, L. Olsson, Appl. Catal. B-Environ. 160–161 (2014) 480–491.
[17] I.X. Green, W.J. Tang, M. Neurock, J.T. Yates, Science 333 (2011) 736–739.
[18] A.A. Herzing, C.J. Kiely, A.F. Carley, P. Landon, G.J. Hutchings, Science 321 (2008) 1331–1335.
[19] W. Grünert, D. Großmann, H. Noei, M.-M. Pohl, I. Sinev, A. De Toni, Y. Wang, M. Muhler, Angew. Chem. Int. Ed. 53 (2014) 3245–3249.
[20] D. Widmann, R.J. Behm, Angew. Chem. Int. Ed. 50 (2011) 10241–10245.
[21] M. Kotobuki, R. Leppelt, D.A. Hansgen, D. Widmann, R.J. Behm, J. Catal. 264 (2009) 67–76.
[22] D. Miller, H. Sanchez Casalongue, H. Bluhm, H. Ogasawara, A. Nilsson, S. Kaya, J. Am. Chem. Soc. 136 (2014) 6340–6347.
[23] J. Guzman, S. Carrettin, A. Corma, J. Am. Chem. Soc. 127 (2005) 3286–3287.
[24] T. Fujitani, I. Nakamura, Angew. Chem. Int. Ed. 50 (2011) 10144–10147.
[25] N.K. Gamboa-Rosales, J.L. Ayastuy, Z. Boukha, N. Bion, D. Duprez, J.A. Pérez-Omil, E. del Río, M.A. Gutiérrez-Ortiz, Appl. Catal. B-Environ. 168–169 (2015) 87–97.
[26] L. Li, X.C. Zeng, J. Am. Chem. Soc. 136 (2014) 15857–15860.
[27] G. Chen, Y. Zhao, G. Fu, P.N. Duchesne, L. Gu, Y. Zheng, X. Weng, M. Chen, P. Zhang, C.W. Pao, J.F. Lee, N. Zheng, Science 344 (2014) 495–499.
[28] Q. Fu, W.-X. Li, Y. Yao, H. Liu, H.-Y. Su, D. Ma, X.-K. Gu, L. Chen, Z. Wang, H. Zhang, B. Wang, X. Bao, Science 328 (2010) 1141–1144.
[29] H. Zhang, D. Lin, G. Xu, J. Zheng, N. Zhang, Y. Li, B.H. Chen, Int. J. Hydrogen Energy 40 (2015) 1742–1751.
[30] X. Guo, Q. Fu, Y. Ning, M. Wei, M. Li, S. Zhang, Z. Jiang, X. Bao, J. Am. Chem. Soc. 134 (2012) 12350–12353.
[31] R. Ferrando, J. Jellinek, R.L. Johnston, Chem. Rev. 108 (2008) 845–910.
[32] Y. Yu, W. Yang, X. Sun, W. Zhu, X.Z. Li, D.J. Sellmyer, S. Sun, Nano Lett. 14 (2014) 2778–2782.
[33] S. Sun, C.B. Murray, D. Weller, L. Folks, A. Moser, Science 287 (2000) 1989–1992.
[34] M.E. Grass, Y.W. Zhang, D.R. Butcher, J.Y. Park, Y.M. Li, H. Bluhm, K.M. Bratlie, T.F. Zhang, G.A. Somorjai, Angew. Chem. Int. Ed. 47 (2008) 8893–8896.
[35] J. Chen, T. Herricks, M. Geissler, Y. Xia, J. Am. Chem. Soc. 126 (2004) 10854–10855.
[36] H.H. Brongersma, M. Draxler, M. de Ridder, P. Bauer, Surf. Sci. Rep. 62 (2007) 63–109.
[37] X. Li, W.-X. Chen, J. Zhao, W. Xing, Z.-D. Xu, Carbon 43 (2005) 2168–2174.
[38] W. Yu, W. Tu, H. Liu, Langmuir 15 (1998) 6–9.
[39] C. Bock, C. Paquet, M. Couillard, G.A. Botton, B.R. MacDougall, J. Am. Chem. Soc. 126 (2004) 8028–8037.
[40] A.U. Nilekar, S. Alayoglu, B. Eichhorn, M. Mavrikakis, J. Am. Chem. Soc. 132 (2010) 7418–7428.
[41] H. Zhang, M. Jin, H. Liu, J. Wang, M.J. Kim, D. Yang, Z. Xie, J. Liu, Y. Xia, ACS Nano 5 (2011) 8212–8222.

[42] T. Komatsu, M. Takasaki, K. Ozawa, S. Furukawa, A. Muramatsu, J. Phys. Chem. C 117 (2013) 10483–10491.
[43] E.-Y. Ko, E.D. Park, H.C. Lee, D. Lee, S. Kim, Angew. Chem. Int. Ed. 46 (2007) 734–737.
[44] C. Lemire, R. Meyer, S. Shaikhutdinov, H.-J. Freund, Angew. Chem. Int. Ed. 43 (2004) 118–121.
[45] H. Iida, A. Igarashi, Appl. Catal. A-Gen. 298 (2006) 152–160.
[46] A. Tanksale, J.N. Beltramini, J.A. Dumesic, G.Q. Lu, J. Catal. 258 (2008) 366–377.
[47] I.X. Green, W. Tang, M. Neurock, J.T. Yates, Science 333 (2011) 736–739.
[48] P.O. Graf, D.J.M. de Vlieger, B.L. Mojet, L. Lefferts, J. Catal. 262 (2009) 181–187.
[49] P.-A. Carlsson, L. Österlund, P. Thormählen, A. Palmqvist, E. Fridell, J. Jansson, M. Skoglundh, J. Catal. 226 (2004) 422–434.
[50] X. Su, P.S. Cremer, Y.R. Shen, G.A. Somorjai, J. Am. Chem. Soc. 119 (1997) 3994–4000.
[51] E. Becker, P.-A. Carlsson, L. Kylhammar, M.A. Newton, M. Skoglundh, J. Phys. Chem. C 115 (2010) 944–951.
[52] H. Song, R.M. Rioux, J.D. Hoefelmeyer, R. Komor, K. Niesz, M. Grass, P. Yang, G.A. Somorjai, J. Am. Chem. Soc. 128 (2006) 3027–3037.
[53] J. Xu, X.-C. Xu, L. Ouyang, X.-J. Yang, W. Mao, J. Su, Y.-F. Han, J. Catal. 287 (2012) 114–123.
[54] X. Liu, O. Korotkikh, R. Farrauto, Appl. Catal. A-Gen. 226 (2002) 293–303.
[55] L.R. Merte, M. Ahmadi, F. Behafarid, L.K. Ono, E. Lira, J. Matos, L. Li, J.C. Yang, B. Roldan Cuenya, ACS Catal. 3 (2013) 1460–1468.
[56] S. Zhang, J.-J. Shan, Y. Zhu, A.I. Frenkel, A. Patlolla, W. Huang, S.J. Yoon, L. Wang, H. Yoshida, S. Takeda, F. Tao, J. Am. Chem. Soc. 135 (2013) 8283–8293.
[57] J. Blanco, A.L. Petre, M. Yates, M.P. Martin, S. Suarez, J.A. Martin, Adv. Mater. 18 (2006) 1162–1165.
[58] T. Yamashita, P. Hayes, Appl. Surf. Sci. 254 (2008) 2441–2449.
[59] J.P. Stassi, P.D. Zgolicz, S.R. de Miguel, O.A. Scelza, J. Catal. 306 (2013) 11–29.
[60] X. Deng, J. Lee, C. Wang, C. Matranga, F. Aksoy, Z. Liu, Langmuir 27 (2011) 2146–2149.
[61] Y.J. Kim, C. Westphal, R.X. Ynzunza, Z. Wang, H.C. Galloway, M. Salmeron, M.A. Van Hove, C.S. Fadley, Surf. Sci. 416 (1998) 68–111.
[62] B. Li, J. Wang, Y. Yuan, H. Ariga, S. Takakusagi, K. Asakura, ACS Catal. 1 (2011) 1521–1528.
[63] Q. Fu, Y. Yao, X. Guo, M. Wei, Y. Ning, H. Liu, F. Yang, Z. Liu, X. Bao, Phys. Chem. Chem. Phys. 15 (2013) 14708–14714.
[64] M.M. Schubert, S. Hackenberg, A.C. van Veen, M. Muhler, V. Plzak, R.J. Behm, J. Catal. 197 (2001) 113–122.
[65] D. Widmann, Y. Liu, F. Schüth, R.J. Behm, J. Catal. 276 (2010) 292–305.
[66] L. Yang, S. Shan, R. Loukrakpam, V. Petkov, Y. Ren, B.N. Wanjala, M.H. Engelhard, J. Luo, J. Yin, Y. Chen, C.-J. Zhong, J. Am. Chem. Soc. 134 (2012) 15048–15060.
[67] W. Göpel, G. Rocker, R. Feierabend, Phys. Rev. B 28 (1983) 3427–3438.
[68] W.-P. Dow, T.-J. Huang, J. Catal. 160 (1996) 171–182.
[69] A. Lewera, L. Timperman, A. Roguska, N. Alonso-Vante, J. Phys. Chem. C 115 (2011) 20153–20159.